HemoPIC: A Physics-Informed Cerebral Hemodynamics Digital Twin for Brain Perfusion

Yi-Chen Lee and Peirong Liu*

Department of Electrical and Computer Engineering,
Data Science and AI Institute,
Johns Hopkins University

{ylee268,pliu53}@jh.edu

Abstract. Perfusion imaging guides clinical evaluation of stroke and brain tumors by characterizing tissue-level hemodynamics. Routine quantification relies on manual arterial input function (AIF) selection followed by deconvolution, producing summary maps without an executable temporal model for simulation or mechanistic insight. Tracer-dynamics-based models infer transport or compartmental parameters from perfusion time series, but do not yield clinically actionable perfusion indices (e.g., CBF, CBV, MTT) that inform diagnosis and treatment decisions. In this work, we propose HemoPIC, a physics-informed cerebral hemodynamics digital twin that explains perfusion time series through tracer mass conservation and a lumped parameter hemodynamic model. Specifically, HemoPIC solves a constrained inverse problem that jointly estimates digital twin parameters and latent states from perfusion imaging, eliminating manual AIF selection and deconvolution from routine perfusion quantification while directly producing clinically actionable perfusion summary maps. Experiments demonstrate that HemoPIC reconstructs tracer dynamics, generates physiologically consistent perfusion maps with lesion hypoperfusion patterns, satisfies central volume consistency, and yields a mechanistic hemodynamic digital twin. Code is publicly available at https://github.com/jhuldr/HemoPIC.

Keywords: Physics-Informed Digital Twin · Brain Perfusion · Stroke

1 Introduction

Medical digital twins construct patient-specific models that link clinical observations to latent physiological states. A standard twin supports patient monitoring, forecasting, and risk stratification. A physics-informed twin goes further. It encodes conservation laws and physiologic dynamics, enabling forward simulations, backward inference to reveal the physiology underlying clinical observations, and counterfactual evaluation of hypothetical interventions. Although digital twins have been explored for organs such as the heart, lung, and liver [10,14], cerebral

* Corresponding author.

digital twins remain underexplored, largely due to the brain's structural complexity and the identifiability bottleneck under routine clinical measurements. In particular, variability in the Circle of Willis and collateral flow pathways complicates reliable inference of regional perfusion under occlusion [9].

Perfusion imaging, such as dynamic susceptibility contrast (DSC) MRI which measures cerebral blood flow via intravascular tracer injections, is widely used to assess cerebral perfusion and vascular permeability in stroke, brain tumors, and neurodegeneration [6,11]. Clinically, perfusion image analysis typically derives spatial summary maps, such as cerebral blood flow (CBF), cerebral blood volume (CBV), and mean transit time (MTT), from the observed tracer time series using voxelwise kinetic modeling [8]. However, this process requires manual selection of an arterial input function (AIF) followed by deconvolution, a sensitive inverse approximation step that could introduce substantial variability in the resulting perfusion summary maps [15]. Because treatment decisions (e.g., thrombectomy) rely on static thresholding of these maps [1], small algorithmic differences can lead to large discrepancies in penumbra estimation and potentially inconsistent clinical decisions. Deep-learning-based models have shown promise in improving the speed, robustness, and accuracy of conventional perfusion-map computation [5,13,24,25]. Nevertheless, the conventional AIF-based pipeline ultimately produces summary maps rather than an explicit hemodynamic state evolution governed by physical dynamics. This limits their utility for broader patient-specific modeling, temporal prediction, and potential action-enabled treatment simulation [19].

Several recent efforts move beyond static map-based postprocessing by incorporating physics-based modeling. Tracer transport approaches [17,18,19,20] fit an advection-diffusion model, governed by spatially varying blood velocity and diffusion fields, directly to the spatiotemporal tracer dynamics. These approaches enforce a physical law and capture spatial coupling beyond voxelwise kinetic fitting. Quantitative transport mapping [28] applies a conservation law tracer transport model to infer flow-related fields from dynamic imaging, demonstrated in the kidney with multi-delay arterial spin labeling and angiography-informed vascular priors, and in the liver with dynamic contrast-enhanced (DCE) MRI [23]. These transport-derived fields can be estimated without manual AIF selection. However, translating them into clinically actionable perfusion indices such as CBF remains nontrivial. One notable exception is [3], which formulates a physics-informed cerebral hemodynamics digital twin with latent states defined directly in volumetric CBF; however, it requires multimodal bedside monitoring signals, including arterial blood pressure (ABP), intracranial pressure (ICP), transcranial Doppler [4], and end-tidal carbon dioxide [16], in addition to perfusion imaging. These signals are not standardized in routine clinical practice.

Contribution: In this work, we introduce HemoPIC: a Physics-Informed Cerebral Hemodynamics digital twin constructed from routine perfusion imaging alone. HemoPIC infers temporal hemodynamic latent states that govern the full tracer inflow-outflow passage and enable forward simulation. By introducing a lumped terminal hemodynamic closure on spatially aggregated tracer dynamics,

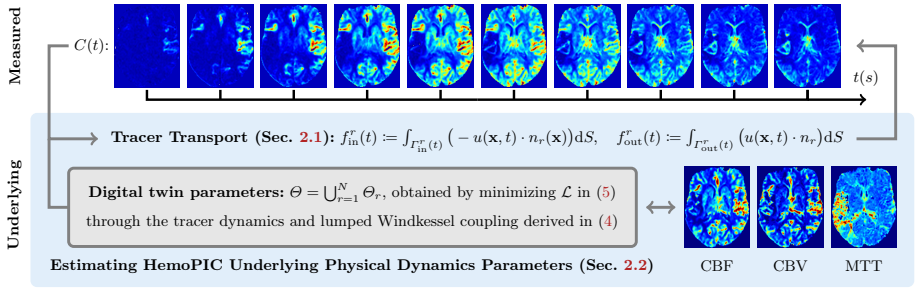

Fig. 1. HemoPIC overview. Given measured tracer dynamics, HemoPIC estimates regional blood inflow (f^r_{in}) and outflow (f^r_{out}) without requiring AIF, by coupling tracer transport with patient-specific hemodynamics in a physics-grounded formulation.

HemoPIC links blood inflow, cerebrovascular storage, and blood outflow within a compact physical structure without patient-specific outlet conditions. Notably, HemoPIC eliminates manual AIF selection, bypasses deconvolution pipelines, and yields hemodynamic latent state estimates that directly lead to clinically interpretable perfusion summary maps. Experiments show that HemoPIC generates clinically consistent perfusion summary maps, satisfies central volume theorem consistency, and reveals underlying Windkessel dynamics. Importantly, it is the first method to reconstruct the complete inflow–outflow tracer passage.

2 Patient-Specific Hemodynamic Digital Twin for Cerebral Perfusion via Tracer Transport

Sec. 2.1 formulates the forward model that links perfusion tracer dynamics with a lumped Windkessel model. Sec. 2.2 presents a parameter inference procedure by solving the resulting composite inverse problem from observed tracer dynamics. Fig. 1 provides an overview of the HemoPIC framework.

2.1 Regional Cerebral Inflow-Outflow Model Formulation

High-dimensional cerebrovascular simulations solve incompressible conservation laws to estimate intravascular blood flow velocity and pressure fields, but their predictions are highly sensitive to boundary conditions, with inlet waveforms and physiological assumptions significantly influencing hemodynamic outputs [22,27]. Furthermore, intravascular fields alone do not directly yield clinical perfusion indices (e.g., CBF) without additional tracer kinetic modeling [8,21], and outlet boundary conditions typically require terminal lumped resistance models [12].

To mitigate this boundary-condition sensitivity, we adopt a regionally aggregated formulation. Specifically, we consider a partition of the brain domain $\Omega \subset \mathbb{R}^3$ into N disjoint subsets $\{\Omega_r\}_{r=1}^N$, such that $\Omega = \bigcup_{r=1}^N \Omega_r$. Each subset Ω_r denotes a spatial cluster with boundary $\partial\Omega_r$ and an associated outward unit

normal vector $n_r(\mathbf{x})$ for $\mathbf{x} \in \partial\Omega_r$. These subsets correspond to subject-specific anatomical units, such as vascular compartments defined by tissue geometry and structural segmentation [2]. Let $u(\mathbf{x},t) \coloneqq (u^x(\mathbf{x},t), u^y(\mathbf{x},t), u^z(\mathbf{x},t))^\top$ denote the spatiotemporal blood flow velocity in directions x, y, z, respectively. For a given Ω_r, we partition the boundary as $\partial\Omega_r = \Gamma^r_{\text{in}}(t) \cup \Gamma^r_{\text{out}}(t)$, where $\Gamma^r_{\text{in}}(t)$ and $\Gamma^r_{\text{out}}(t)$ denote the boundary of blood inflow and outflow, respectively,

$$\Gamma^r_{\text{in}}(t) \coloneqq \big\{\mathbf{x} \in \partial\Omega_r : u(\mathbf{x},t)\cdot n_r < 0\big\}, \quad \Gamma^r_{\text{out}}(t) \coloneqq \big\{\mathbf{x} \in \partial\Omega_r : u(\mathbf{x},t)\cdot n_r > 0\big\}.$$

We then define the effective volumetric inflow and outflow rates for Ω_r by

$$f^r_{\text{in}}(t) \coloneqq \int_{\Gamma^r_{\text{in}}(t)} \big(-u(\mathbf{x},t)\cdot n_r(\mathbf{x})\big)\mathrm{d}S, \quad f^r_{\text{out}}(t) \coloneqq \int_{\Gamma^r_{\text{out}}(t)} \big(u(\mathbf{x},t)\cdot n_r\big)\mathrm{d}S.$$

Lumped Windkessel Model. To link regional inflow and outflow without subject-specific outlet boundary data, we incorporate a two-element Windkessel model as a terminal impedance boundary condition for each tracer compartment. Specifically, for each partition Ω_r, the model couples the effective inflow and outflow rates $(f^r_{\text{in}}(t), f^r_{\text{out}}(t))$ through regional lumped parameters $\theta^r = (\theta^r_W, \theta^r_R)$,

$$\theta^r_W \frac{\mathrm{d}}{\mathrm{d}t}(P^r(t) - P^r_v) = f^r_{\text{in}}(t) - f^r_{\text{out}}(t), \quad f^r_{\text{out}}(t) = \frac{P^r(t) - P^r_v}{\theta^r_R},$$

where $P^r(t)$ denotes an effective microvascular pressure state, P^r_v denotes a constant downstream reference pressure, $\theta^r_R > 0$ denotes an effective resistance, and $\theta^r_W > 0$ denotes an effective compliance. Equivalently, we have the expression:

$$f^r_{\text{out}}(t) = f^r_{\text{out}}(0)\exp\left(-\frac{t}{\tau^r}\right) + \frac{1}{\tau^r}\int_0^t \exp\left(\frac{s-t}{\tau^r}\right) f^r_{\text{in}}(s)\mathrm{d}s, \tag{1}$$

where $\tau^r = \theta^r_W \cdot \theta^r_R$. Within each partition Ω_r, θ^r_W represents vascular compliance (blood storage), θ^r_R represents resistance (blood discharge), and product τ^r sets the characteristic relaxation time governing outflow response to inflow changes.

Tracer Dynamics. We further link the above regional inflow-outflow formulation to perfusion tracer dynamics. Let $C_r(\mathbf{x},t)$ denote the tracer concentration at $\mathbf{x} \in \Omega_r$, at time t. The advection-diffusion equation [18,19] gives:

$$\frac{\partial C_r(\mathbf{x},t)}{\partial t} = -\nabla\cdot(u(\mathbf{x},t)C_r(\mathbf{x},t)) + \nabla\cdot(D(\mathbf{x},t)\nabla C_r(\mathbf{x},t)), \tag{2}$$

where D governs the tracer's diffusion. Integrating both sides over Ω_r and applying the divergence theorem, the right-hand side of (2) becomes:

$$\underbrace{-\int_{\partial\Omega_r}(u(\mathbf{x},t)C_r(\mathbf{x},t))\cdot n_r\mathrm{d}S}_{\coloneqq \Phi^r_A(t)} + \underbrace{\int_{\partial\Omega_r}(D(\mathbf{x},t)\nabla C_r(\mathbf{x},t))\cdot n_r\mathrm{d}S}_{\coloneqq \Phi^r_D(t)}, \tag{3}$$

where $\Phi_A^r(t)$ admits the decomposition:

$$\Phi_A^r(t) = -\int_{\Gamma_{\text{out}}^r(t)} (u(\mathbf{x},t)\cdot n_r) C_r(\mathbf{x},t)\mathrm{d}S - \int_{\Gamma_{\text{in}}^r(t)} (u(\mathbf{x},t)\cdot n_r) C_r(\mathbf{x},t)\mathrm{d}S.$$

To compactly represent the advective flux, we define the weighted concentration flux, with a minus sign for inflow and a plus sign for outflow:

$$C_{\text{in/out}}^r(t) \coloneqq \frac{1}{f_{\text{in/out}}^r(t)} \cdot \int_{\Gamma_{\text{in/out}}^r(t)} \pm\,(u(\mathbf{x},t)\cdot n_r(\mathbf{x})) C_r(\mathbf{x},t)\,\mathrm{d}S.$$

For an effective distribution volume V_r, we define the cluster level state average concentration $\bar{C}_r(t) \coloneqq \frac{1}{V_r}\int_{\Omega_r} C_r(\mathbf{x},t)\mathrm{d}\mathbf{x}$. Then, (3) becomes

$$\frac{\mathrm{d}}{\mathrm{d}t}(V_r \bar{C}_r(t)) = f_{\text{in}}^r(t) C_{\text{in}}^r(t) - f_{\text{out}}^r(t) C_{\text{out}}^r(t) + \Phi_D^r(t). \tag{4}$$

Regional integration converts the diffusion term in [18,19] into a net boundary-flux residual rather than a voxelwise field. We thus set $\Phi_D^r = 0$ in (4) $\forall r$, assuming that effective inflow, outflow, and storage capture regional tracer exchange.

2.2 Estimating Underlying Physical Dynamics Parameters

Here, we formulate the parameter-estimation problem for the digital twin in Sec. 2.1 from perfusion-derived volumetric tracer time series. Since perfusion source data do not uniquely identify region-specific inflow rates and boundary conditions, we adopt a reduced parameterization that preserves the characteristic relaxation scale of the Windkessel, while keeping the inverse problem identifiable. Specifically, for $r \in [N]$, we compute the regional mean concentration $\{\bar{C}_r(t) \mid t \in [T]\}$ by averaging voxelwise concentrations within each region, and consider a regional constant inflow $f_{\text{in}}^r(t) = F_r$. We represent the inflow concentration through a region-specific amplitude $\bar{C}_{\text{in}}^r > 0$, modulating a shared inflow shape $C_{\text{in}}^r(t) = \bar{C}_{\text{in}}^r \cdot C_{\text{art}}(t)$, where $C_{\text{art}}(t)$ is a unit peak arterial proxy curve shared across clusters. The resulting composite model contains two parts. First, the lumped Windkessel model computes the blood outflow $\hat{f}_{\text{out}}^r(t)$ from $(F_r, \theta_W^r, \theta_R^r)$ under a fixed initial condition (1). Second, the reduced tracer compartment yields the regional concentration $\hat{C}_r(t)$ with $(V_r, C_{\text{in}}^r(t), \hat{f}_{\text{out}}^r(t))$. Together, we estimate the digital twin parameters, $\Theta = \bigcup_{r=1}^N \Theta_r$, where $\Theta_r = \{\theta_W^r, \theta_R^r, V_r, F_r, \bar{C}_{\text{in}}^r\}$, by minimizing the following loss with regularization coefficients $\lambda_{\text{in}}, \lambda_V, \lambda_F, \lambda_R$:

$$\mathcal{L} = \sum_{r=1}^{N} \frac{\sum_{t=1}^{T} \omega(t)\big(\hat{C}_r(t;\Theta_r) - \bar{C}_r(t)\big)^2}{\sum_{t=1}^{T} \omega(t)\bar{C}_r(t)^2 + \epsilon} + \lambda_{\text{in}}\mathcal{L}_{\text{in}} + \lambda_V\mathcal{L}_V + \lambda_F\mathcal{L}_F + \lambda_R\mathcal{L}_R, \tag{5}$$

subject to $\theta_R^r, \theta_W^r, F_r, V_r, \bar{C}_{\text{in}}^r > 0$ for all r, where $\omega(\cdot)$ is a positive time weight that modulates each time point's contribution, $\mathcal{L}_{\text{in}} = \sum_r (\log \bar{C}_{\text{in}}^r - \log C_{\text{prior}}^r)^2$, $\mathcal{L}_V = \sum_r (\log V_r - \log V_r^{\text{prior}})^2$ and $\mathcal{L}_F = \sum_r (\log F_r - \log F_r^{\text{prior}})^2$ with positive priors $\bar{C}_{\text{prior}}^r, V_r^{\text{prior}}$ and F_r^{prior} derived from data to stabilize the inverse problem. We additionally apply $\mathcal{L}_R = \sum_r (\log \theta_R^r - \log \theta_R^0)^2$, where $\theta_R^0 > 0$ is a fixed reference resistance used to avoid extreme values under limited identifiability.

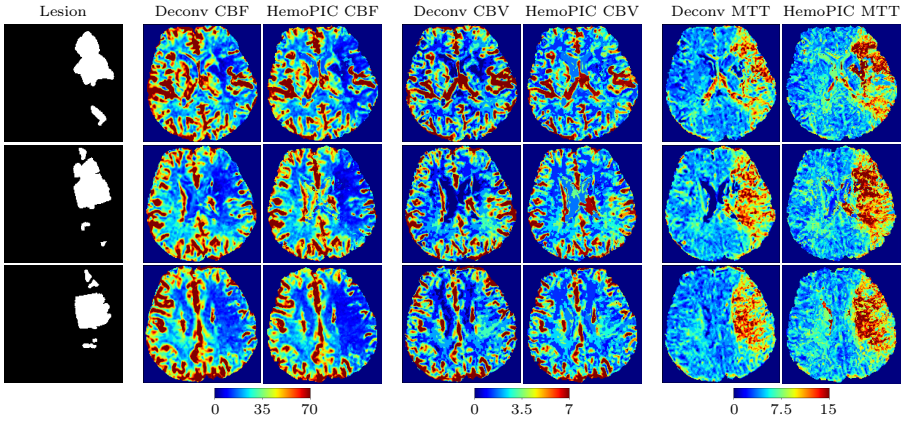

Fig. 2. Qualitative comparison of ISLES 2017 silver-standard, AIF-based deconvolution maps and HemoPIC-derived maps, shown with identical scales for each parameter.

3 Experiments

We evaluate HemoPIC on the ISLES 2017 acute ischemic stroke dataset [26], consisting of 44 patients with 4D DSC-MRI perfusion images, deconvolution-derived perfusion maps (CBF, CBV, MTT), and gold-standard expert-annotated lesion masks. MR signals are converted to voxelwise tracer concentration [8].

To obtain anatomically meaningful partitions $\{\Omega_r\}_{r=1}^{N}$, we apply SynthSeg [2] to segment grey matter (GM), white matter (WM), cerebrospinal fluid (CSF), and brain stem. GM and WM are further divided using k-means on tracer time-curve features (8 clusters for GM, 6 for WM), and neighboring clusters with fewer than 400 voxels are merged. For each Ω_r, parameters are fitted from the regional mean concentration curve. A global arterial curve $C_{\text{art}}(t)$ is constructed from high-peak time curves, smoothed (Gaussian std = 1.8), and peak-normalized. F_r^{prior} (V_r^{prior}) is set from median CBF (CBV) within Ω_r, $\bar{C}_{\text{prior}}^r$ is set from the peak of smoothed $C_r(t)$. We optimize using Powell's method with $\lambda_{\text{in}} = 0.06$, $\lambda_V = \lambda_F = 0.04$, $\lambda_R = 0.002$, $\theta_R^0 = 1$. Loss weights $\omega(t)$ are set as $0.2{+}0.8C_{\text{art}}(t)$, restricting evaluation to time points with $\omega(t) \geq 0.2$ to emphasize tracer passage.

3.1 Consistency and Comparison with AIF-based Silver Standards

We first compare the perfusion summary maps (CBF, CBV, MTT) from conventional deconvolution-based methods and HemoPIC. We report regional CBF and CBV on the same numerical scale conventionally used in deconvolution-based models. MTT is reported in seconds. We set the regional mean CBF in Ω_r to the mean over the last 20% of the estimated blood outflow $\hat{f}_{\text{out}}^r(t)$, then modulate it voxelwise within Ω_r using each voxel's tracer curve to capture within-cluster heterogeneity, excluding non-parenchymal regions. Similarly, we set the regional mean CBV in Ω_r to the estimated effective volume V_r, and distribute it voxelwise

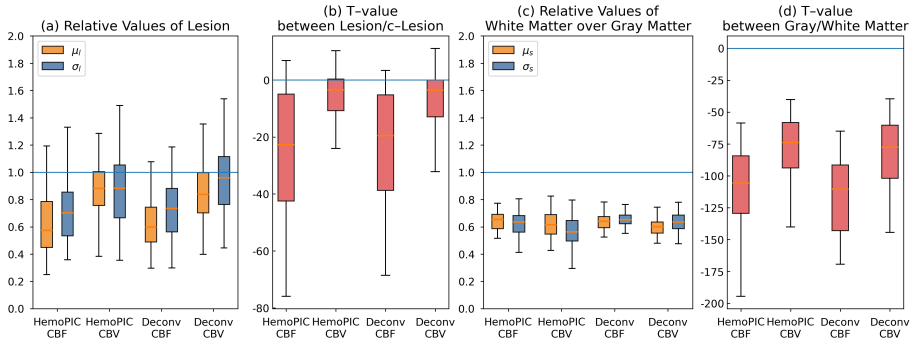

Fig. 3. Box plots comparing HemoPIC and deconvolution-based (Deconv) maps (lower is better). Relative mean and std for lesion vs. c-lesion (a), and WM vs. GM (c). Corresponding unpaired t-value for lesion vs. c-lesion (b), and WM vs. GM (d).

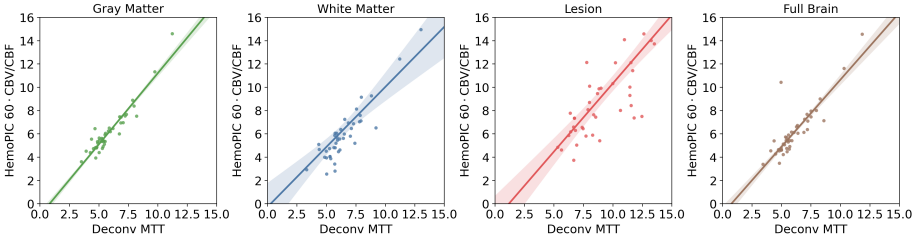

Fig. 4. Regional central volume theorem consistency verification. Dots: patient-level regional means. Lines/shading: region-wise OLS fits across 44 patients with ± standard error bands. Slopes: 1.22 (GM), 1.03 (WM), 1.17 (Lesion), and 1.15 (Full Brain).

within Ω_r using the relative pattern of the data CBV map after clipping and mean normalization. MTT is computed by the relation $\text{MTT} = 60 \cdot \text{CBV}/\text{CBF}$.

Perfusion Summary Maps and Downstream Lesion Identification. Fig. 2 compares silver-standard reference perfusion maps from conventional deconvolution-based approaches [26] with HemoPIC-derived maps using identical scales. HemoPIC maps closely match the scale and spatial patterns of the silver-standard references while providing stronger lesion contrast. ROC analysis further showed that HemoPIC matched or exceeded the silver-standard reference maps across all perfusion parameters, with AUCs of 0.76 vs. 0.75 for CBF, 0.58 vs. 0.58 for CBV, and 0.72 vs. 0.69 for MTT. These results indicate that HemoPIC preserves lesion-relevant perfusion contrast while avoiding the AIF-selection sensitivity of conventional AIF-based deconvolution pipelines [15].

Fig. 3 reports the relative mean, standard deviation, and unpaired t-statistic between voxel values for each region pair. Following [18,19], we define μ_s and σ_s as the WM-to-GM ratios of regional mean and standard deviation, and μ_l and σ_l as the corresponding lesion-to-contralateral-lesion ratios, where the contralateral

Table 1. Cohort summary of normalized root mean square error for tracer concentration reconstruction ($N = 44$). Q25 and Q75 denote the 25th and the 75th percentiles..

Stats	GM	WM	Lesion	c-Lesion	Full brain
mean ± std	0.106±0.045	0.095±0.068	0.318±0.291	0.192±0.104	0.093±0.057
median	0.099	0.083	0.266	0.176	0.083
[Q25, Q75]	[0.085,0.108]	[0.066,0.095]	[0.162,0.361]	[0.148,0.210]	[0.075,0.088]

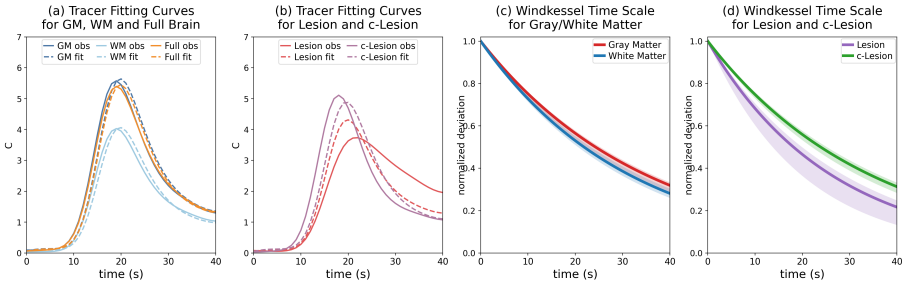

Fig. 5. (a)-(b) Cohort-mean observed (solid) and reconstructed (dashed) tracer concentration time curves. (c)-(d) Windkessel time scales with voxel-weighted median (thick) and 40th–60th percentile band over the four regions across all 44 patients.

lesion (c-lesion) is obtained by hemispheric mirroring. Lower values indicate better performance. Specifically, $\mu_s < 1$ reflects higher mean CBF in GM than WM, consistent with healthy perfusion physiology [7], while $\mu_l < 1$ reflects lesion hypoperfusion relative to the contralateral region [18,19].

Regional Central Volume Theorem Consistency. We further assess the consistency of the regional central volume theorem between HemoPIC and clinical perfusion summary maps. Fig. 4 compares the deconvolution-derived regional mean MTT against the regional mean $60 \cdot \mathrm{CBV}/\mathrm{CBF}$ from HemoPIC across all patients, in GM, WM, Lesion, and Full Brain. The scatter is approximately linear with slopes near one across regions, indicating quantitative agreement with the clinical MTT scale and the indicator dilution identity $\mathrm{MTT} = \mathrm{CBV}/\mathrm{CBF}$ [21,29].

3.2 Unique Capabilities of HemoPIC

Full Tracer Passage Reconstruction. Fig. 5 compares the observed regional mean concentration time curves and the reconstructed curves for GM, WM, lesion, the contralateral region of the lesion (c-lesion), and full brain. Notably, prior tracer dynamics estimation models [18,19,20] only estimate the outflow phase after the global time-to-peak. In contrast, HemoPIC reconstructs full tracer dynamics by estimating hemodynamic states that capture both inflow and outflow.

Windkessel Dynamics. We further report HemoPIC digital twin parameters that govern the regional Windkessel outflow dynamics through their product

$\tau^r = \theta_W^r \theta_R^r$, which defines the characteristic relaxation time scale of (1). Assuming $f_{\text{in}}^r(t) \approx F^r$, deviations of $f_{\text{out}}^r(t)$ decay as $\exp(-t/\tau^r)$. We therefore report the normalized decay curve. Fig. 5 pools ROI-level τ^r across patients within each tissue group using voxelwise weights, showing the decay curve induced by the weighted median (thick line) and the 40th–60th percentile range (shaded band). GM and WM exhibit similar relaxation (medians 13.95 s and 12.56 s). Lesions relax faster than contralateral tissue (medians 10.41 s vs. 13.71 s).

4 Conclusion

We propose HemoPIC, a physics-informed digital twin for cerebral perfusion that couples hemodynamic modeling with tracer transport to infer patient-specific flow and volume parameters from routine perfusion imaging. Beyond reconstructing full inflow–outflow tracer dynamics, HemoPIC generates clinically consistent perfusion maps without requiring AIF selection. To our knowledge, HemoPIC is the first approach to connect tracer transport modeling with clinically standard perfusion indices, providing a novel foundation for physics-grounded, fully automated stroke assessment and simulation-driven clinical decision support.

Disclosure of Interests. The authors declare no competing interests.

References

1. Albers, G.W., Marks, M.P., Kemp, S., Christensen, S., Tsai, J.P., Ortega-Gutierrez, S., McTaggart, R.A., Torbey, M.T., Kim-Tenser, M., Leslie-Mazwi, T., et al.: Thrombectomy for stroke at 6 to 16 hours with selection by perfusion imaging. New England Journal of Medicine (2018)
2. Billot, B., Greve, D.N., Puonti, O., Thielscher, A., Van Leemput, K., Fischl, B., Dalca, A.V., Iglesias, J.E., et al.: SynthSeg: Segmentation of brain MRI scans of any contrast and resolution without retraining. Medical image analysis (2023)
3. Briggs, J.K., Stroh, J., Park, S., Foreman, B., Tymko, M.M., Carr, J., Sirlanci, M., Ainslie, P.N., Benninger, R.K., Bennett, T.D., et al.: Towards a physics informed digital twin to predict cerebral blood flow and cerebral vascular regulation. npj Digital Medicine (2026)
4. Claassen, J.A., Zhang, R., Fu, Q., Witkowski, S., Levine, B.D.: Transcranial Doppler estimation of cerebral blood flow and cerebrovascular conductance during modified rebreathing. Journal of applied physiology (2007)
5. De Vries, L., Van Herten, R.L., Hoving, J.W., Išgum, I., Emmer, B.J., Majoie, C.B., Marquering, H.A., Gavves, E.: Spatio-temporal physics-informed learning: A novel approach to CT perfusion analysis in acute ischemic stroke. Medical image analysis (2023)
6. Desai, B.S., Monahan, A.J., Carvey, P.M., Hendey, B.: Blood–brain barrier pathology in Alzheimer's and Parkinson's disease: implications for drug therapy. Cell transplantation (2007)
7. Fantini, S., Sassaroli, A., Tgavalekos, K.T., Kornbluth, J.: Cerebral blood flow and autoregulation: current measurement techniques and prospects for noninvasive optical methods. Neurophotonics (2016)

8. Fieselmann, A., Kowarschik, M., Ganguly, A., Hornegger, J., Fahrig, R.: Deconvolution-based CT and MR brain perfusion measurement: theoretical model revisited and practical implementation details. International Journal of Biomedical Imaging (2011)
9. Hoksbergen, A., Fulesdi, B., Legemate, D., Csiba, L.: Collateral configuration of the circle of Willis: transcranial color-coded duplex ultrasonography and comparison with postmortem anatomy. Stroke (2000)
10. Katsoulakis, E., Wang, Q., Wu, H., Shahriyari, L., Fletcher, R., Liu, J., Achenie, L., Liu, H., Jackson, P., Xiao, Y., et al.: Digital twins for health: a scoping review. NPJ digital medicine (2024)
11. Kermode, A., Thompson, A., Tofts, P., MacManus, D., Kendall, B., Kingsley, D., Moseley, I., Rudge, P., McDonald, W.: Breakdown of the blood-brain barrier precedes symptoms and other MRI signs of new lesions in multiple sclerosis: pathogenetic and clinical implications. Brain (1990)
12. Korte, J., Klopp, E.S., Berg, P.: Multi-Dimensional Modeling of Cerebral Hemodynamics: A Systematic Review. Bioengineering (2024)
13. Kuang, H., Qiu, W., Boers, A.M., Brown, S., Muir, K., Majoie, C.B., Dippel, D.W., White, P., Epstein, J., Mitchell, P.J., et al.: Computed tomography perfusion–based machine learning model better predicts follow-up infarction in patients with acute ischemic stroke. stroke (2021)
14. Kuang, K., Dean, F., B Jedlicki, J., Ouyang, D., Philippakis, A., Sontag, D., Alaa, A.M.: Med-real2sim: Non-invasive medical digital twins using physics-informed self-supervised learning. Advances in Neural Information Processing Systems (2024)
15. Kudo, K., Sasaki, M., Yamada, K., Momoshima, S., Utsunomiya, H., Shirato, H., Ogasawara, K.: Differences in CT perfusion maps generated by different commercial software: quantitative analysis by using identical source data of acute stroke patients. Radiology (2010)
16. Levitzky, M.G.: Pulmonary physiology: Lange physiology series. McGraw-Hill Education: New York, NY, USA (2007)
17. Liu, P., Lee, Y., Aylward, S., Niethammer, M.: Deep decomposition for stochastic normal-abnormal transport. In: Proceedings of the IEEE/CVF Conference on Computer Vision and Pattern Recognition (2022)
18. Liu, P., Lee, Y.Z., Aylward, S.R., Niethammer, M.: PIANO: Perfusion imaging via advection-diffusion. In: International Conference on Medical Image Computing and Computer-Assisted Intervention (2020)
19. Liu, P., Lee, Y.Z., Aylward, S.R., Niethammer, M.: Perfusion imaging: an advection diffusion approach. IEEE transactions on medical imaging (2021)
20. Liu, P., Tian, L., Zhang, Y., Aylward, S., Lee, Y., Niethammer, M.: Discovering hidden physics behind transport dynamics. In: Proceedings of the IEEE/CVF Conference on Computer Vision and Pattern Recognition (2021)
21. Meier, P., Zierler, K.L.: On the theory of the indicator-dilution method for measurement of blood flow and volume. Journal of applied physiology (1954)
22. Mut, F., Ruijters, D., Babic, D., Bleise, C., Lylyk, P., Cebral, J.R.: Effects of changing physiologic conditions on the in vivo quantification of hemodynamic variables in cerebral aneurysms treated with flow diverting devices. International Journal for Numerical Methods in Biomedical Engineering (2014)
23. Romano, D., Zhang, Q., Roberts, A.G., Weppner, B., Shou, J., Kovanlikaya, I., S̨is̨man, M., Hu, R., Nguyen, T.D., Dimov, A.V., et al.: Validation of quantitative transport mapping (QTM) with an ex vivo perfused liver model. Magnetic Resonance in Medicine (2025)

24. Soltanpour, M., Greiner, R., Boulanger, P., Buck, B.: Improvement of automatic ischemic stroke lesion segmentation in CT perfusion maps using a learned deep neural network. Computers in biology and medicine (2021)
25. Wang, G., Song, T., Dong, Q., Cui, M., Huang, N., Zhang, S.: Automatic ischemic stroke lesion segmentation from computed tomography perfusion images by image synthesis and attention-based deep neural networks. Medical Image Analysis (2020)
26. Winzeck, S., Hakim, A., McKinley, R., Pinto, J.A., Alves, V., Silva, C., Pisov, M., Krivov, E., Belyaev, M., Monteiro, M., et al.: ISLES 2016 and 2017-benchmarking ischemic stroke lesion outcome prediction based on multispectral MRI. Frontiers in neurology (2018)
27. Xiang, J., Siddiqui, A., Meng, H.: The effect of inlet waveforms on computational hemodynamics of patient-specific intracranial aneurysms. Journal of biomechanics (2014)
28. Zhou, L., Zhang, Q., Spincemaille, P., Nguyen, T.D., Morgan, J., Dai, W., Li, Y., Gupta, A., Prince, M.R., Wang, Y.: Quantitative transport mapping (QTM) of the kidney with an approximate microvascular network. Magnetic resonance in medicine (2021)
29. Zierler, K.: Indicator dilution methods for measuring blood flow, volume, and other properties of biological systems: a brief history and memoir. Annals of biomedical engineering (2000)